Journal of Power Sources 306 (2016) 481–488

Contents lists available at ScienceDirect

Journal of Power Sources

journal homepage: www.elsevier.com/locate/jpowsour

Hierarchical MnO_2 nanowire/graphene hybrid fibers with excellent electrochemical performance for flexible solid-state supercapacitors

Wujun Ma [a, 1], Shaohua Chen [a, 1], Shengyuan Yang [a], Wenping Chen [a], Yanhua Cheng [a], Yiwei Guo [b], Shengjie Peng [c], Seeram Ramakrishna [c], Meifang Zhu [a, *]

[a] State Key Laboratory for Modification of Chemical Fibers and Polymer Materials, College of Materials Science and Engineering, Donghua University, Shanghai 201620, China
[b] Department of Materials Science, Fudan University, Shanghai 200433, China
[c] Centre for Nanofibers and Nanotechnology, National University of Singapore, Singapore 117581, Singapore

HIGHLIGHTS

- Hierarchically structured MnO_2 nanowire/graphene hybrid fibers were fabricated.
- The hybrid fibers possess large specific surface area and high MnO_2 loading.
- The all-solid-state flexible fiber-shaped supercapacitors have been fabricated.
- They exhibit high volumetric capacitance and excellent cycling stability.

GRAPHICAL ABSTRACT

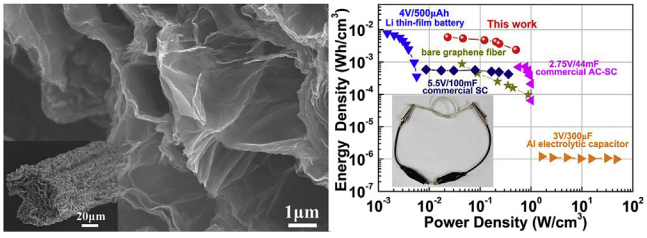

ARTICLE INFO

Article history:
Received 25 September 2015
Received in revised form
15 December 2015
Accepted 17 December 2015
Available online 24 December 2015

Keywords:
Graphene hybrid fiber
MnO_2 nanowires
Wet spinning
Supercapacitors
Wearable electronics\

ABSTRACT

Towards rapid development of lightweight, flexible, and even wearable electronics, a highly efficient energy-storage device is required for their energy supply management. Graphene fiber-based supercapacitor is considered as one of the promising candidates because of the remarkable mechanical and electrical properties of graphene fibers. However, supercapacitors based on bare graphene fibers generally suffer a low capacitance, which certainly restricts their potentially wide applications. In this work, hierarchically structured MnO_2 nanowire/graphene hybrid fibers are fabricated through a simple, scalable wet-spinning method. The hybrid fibers form mesoporous structure with large specific surface area of 139.9 $m^2\ g^{-1}$. The mass loading of MnO_2 can be as high as 40 wt%. Due to the synergistic effect between MnO_2 nanowires and graphene, the main pseudocapacitance of MnO_2 and the electric double-layer capacitance of graphene are improved simultaneously. In view of the practical demonstration, a highly flexible solid-state supercapacitor is fabricated by twisting of two MnO_2/graphene fibers coated by polyvinyl alcohol/H_3PO_4 electrolyte. The supercapacitor exhibits a high volumetric capacitance (66.1 F cm^{-3}, normalized by the total volume of two fiber electrodes), excellent cycling stability (96% capacitance retention over 10,000 cycles), high energy and power density (5.8 mWh cm^{-3} and 0.51 W cm^{-3}, respectively).

1. Introduction

Flexible, lightweight, mechanically strong and highly efficient energy storage devices have attracted significant attention due to

* Corresponding author.
E-mail address: zhumf@dhu.edu.cn (M. Zhu).
[1] These authors contributed equally to this work.

http://dx.doi.org/10.1016/j.jpowsour.2015.12.063
0378-7753/

their potential applications in portable and wearable consumer electronics including electronic papers, roll-up displays, flexible biosensors and implantable medical devices [1–5]. Among various types of energy storage devices, supercapacitors (SCs) have higher power density, longer cycling life, faster charge/discharge rates and safer operation conditions than lithium ion batteries and thus are considered as the most promising energy storage devices [6–9]. The design of flexible SCs needs the advancement of flexible electrodes with favorable mechanical strength and large capacitance. In this point of view, graphene has shown great potential as the electrodes of flexible supercapacitors owing to its distinctive characteristics such as large specific surface area, great mechanical strength and high electrical conductivity. Graphene fiber formed by individual graphene nanosheets is one of the promising candidates as flexible electrodes because of its remarkable mechanical and electrical properties [10–13]. However, due to the aggregating nature of graphene caused by strong $\pi-\pi$ interactions, the graphene nanosheets tend to restack into graphite-like structure during the fabrication process, in which the excellent characteristics of the individual graphene sheet, such as flexibility and high surface area, will be lost [14]. This structure reduces the accessible surface area for ion adsorption/desorption and therefore leads to low specific capacitance and poor rate performance. To overcome these limitations, considerable efforts have been devoted to fabricate porous graphene fibers. For instance, our group prepared porous graphene fibers by a non-liquid-crystal spinning method [12]. Inserting spacers such as CNTs into graphene fiber to expand the layer distance between the individual sheets of graphene fiber is another effective strategy to fabricate porous graphene fibers [15,16]. However, the relatively high production cost of CNTs and non-scalable fabrication process for graphene fibers limit their practical application as electrodes of flexible SCs.

Incorporating pseudocapacitive materials into graphene to form composite is considered as an effective way to improve the capacitance of the electrodes [17–19]. Among the pseudocapacitive materials, manganese dioxide (MnO_2) has attracted much attention due to its low cost, environmental friendliness and high theoretical specific capacitance [20]. By decorating the surface of graphene fibers with MnO_2, Gao et al. [21] and Qu et al. [22] have enhanced the electrochemical performance of the graphene fiber-based electrodes, respectively. However, these methods were complicated and non-scalable. Meanwhile, the capacitance of the hybrid fibers was mainly dominated by the pseudocapacitance from the MnO_2 coated on the graphene fiber surface, and the electric double layer capacitance from the graphene sheet was less utilized due to the agglomerated layer like structure in the graphene fiber. Additionally, due to its low electronic conductivity only a very thin surface layer of MnO_2 can participate in the redox reactions, and further increasing of the mass loading of MnO_2 usually leads to the increased electrode resistance, decreased specific capacitance and reduced utilization rate of MnO_2. Such unfavorable thickness-dependence is a general problem for low conductivity electrode materials and is associated with limitations in the transport of both electrons and ions [23]. Thus, increasing the mass loading content of MnO_2 without sacrificing their utilization rate is still challenging for graphene fibers. In this regard, it is highly desirable to develop a scalable and low-cost approach to fabricate ideal MnO_2/graphene hybrid fibers with outstanding flexibility, high conductivity, large specific surface area and excellent capacitance for flexible SCs.

Here, hierarchically structured MnO_2 nanowires/graphene hybrid fibers with excellent capacitive performance were fabricated by a very simple, low cost and scalable wet-spinning method. The MnO_2 nanowires in these fibers not only act as the effective spacer to inhibit the restacking of graphene nanosheets and increase the specific surface area (139.9 $m^2\ g^{-1}$), but also provide pseudo capacitance to improve the overall performance. Meanwhile, the highly conductive graphene nanosheets wrapping around the MnO_2 nanowires can inhibit the aggregation of MnO_2 nanowires, serve as superhighways facilitating the electron transport in the fiber and increase the mass loading content (as high as 40 wt%) and electrochemical utilization rate of MnO_2. Furthermore, the graphene nanosheets also keep the integrity and stability of the fiber and offer flexibility. Flexible solid-state SCs were assembled using the as-prepared hybrid fibers and they displayed high volumetric capacitance (up to 66.1 F cm^{-3}, normalized by the total volume of two fiber electrodes), excellent cycling stability (96% capacitance retention over 10000 cycles), and high energy and power density (up to 5.8 mWh cm^{-3} and 0.51 W cm^{-3}, respectively). They also well maintained their structure and electrochemical performance under mechanical deformation, indicating a good flexibility of these devices.

2. Experimental section

2.1. Synthesis of MnO_2 nanowires

The MnO_2 nanowires were prepared by a low temperature hydrothermal method. Typically, 0.016 mol $MnSO_4 \cdot H_2O$, 0.016 mol $(NH_4)_2S_2O_8$, 0.03 mol $(NH_4)_2SO_4$ and 0.1 g polyvinylpyrrolidone (PVP) were added into 80 mL distilled water in a beaker under stirring to form a homogeneous solution. The solution was transferred into a Teflonlined stainless steel autoclave, then sealed and maintained at 120 °C for 12 h. After the reaction was completed, the autoclave was cooled to room temperature and the resulting product was filtered, washed with distilled water and ethanol to remove residual salts and finally dried at 120 °C in air.

2.2. Preparation of MnO_2 nanowires/graphene hybrid fibers

Graphite oxide (GO) was synthesized by the Hummers method [24]. To obtain the hybrid fibers, MnO_2 nanowires and GO were mixed at weight ratios of 0:100, 5:95, 10:90, 20:80, 30:70 and 40:60 into distilled water. The mixtures (10 mg/ml) were sonicated for 2 h at an output power of 20 W using a digital ultrasonic processor (S-450D, Branson) and then concentrated to 40 mg/ml by evaporation in 60 °C water bath. These homogeneous dispersions were loaded into plastic syringes and injected into a rotating coagulation bath (acetic acid). The resulted gel fibers were rolled onto a drum and dried at 60 °C in vacuum. To obtain MnO_2/rGO fibers, the as-prepared MnO_2/GO fibers on the drum were put into 2 mL hydrazine solution in a teflon vessel, sealed, then kept at 85 °C for 24 h. The obtained MnO_2/rGO fibers with 5%, 10%, 20%, 30% and 40% MnO_2 loading contents are respectively named as MnO_2/rGO-5 fiber MnO_2/rGO-10 fiber, MnO_2/rGO-20 fiber, MnO_2/rGO-30 fiber and MnO_2/rGO-40 fiber.

2.3. Material characterization

The morphology of the samples was observed by a scanning electron microscope (SEM, HITACHI, S4800) and a transmission electron microscope (TEM, JEOL, JEM-2100F). The X-ray energy disperse spectra (EDS) of the samples were recorded by Oxford Instruments EDS System. The Raman spectra were obtained on a Renishaw microRaman spectroscopy system with a 514.5 nm argon-ion laser. The X-ray diffraction (XRD) patterns were recorded on a D/max 2550 PC diffractometer (Rigaku, Japan) with Cu K radiation (λ = 1.5406 Å) operating at 40 kV and 250 mA. The resistivity was measured by a two probe method on a PC68 high resistance meter (Shanghai Cany Precision Instrument). Tensile tests were carried out at an extension rate of 2 mm min^{-1} with a

gauge length of 10 mm on an XQ-1A fiber tension tester (Shanghai New Fiber Instrument). Nitrogen adsorption–desorption isotherms of the fibers were measured at 77 K using a Micromeritics ASAP2020 static volumetric gas adsorption instrument. The samples were first degassed at 300 °C under high vacuum (<0.01 mbar) before tests. The specific surface area was calculated by the Brunauer–Emmett–Teller (BET) method. The X-ray photoelectron spectra (XPS) were obtained on an Axis Ultra DLD spectrometer (Kratos Analytical, UK) using a monochromatic Al K source.

2.4. Fabrication and characterization of all-solid-state fiber-based SCs

Polyvinyl alcohol (3.0 g) was added to 27.0 g deionized water, followed by heating at 95 °C under magnetic stirring for 3 h H_3PO_4 (3.0 g) was finally dropped to the above solution to form the gel electrolyte. To fabricate a fiber-based SCs, two fibers with the same diameter and length (1 cm) were connected to a metal wire by Ag paste, respectively, immersed in the H_3PO_4-PVA gel solution for 24 h, dried at room temperature until the gel electrolyte solidified, and then carefully twisted together to produce a fiber-based SC. Finally the SC was coated with gel electrolyte again, dried at room temperature, then encapsulated in a silicone tube for ease of test. The electrochemical performances of the assembled SCs were evaluated by cyclic voltammetry (CV) and galvanostatic charge/discharge (GCD) in a two-electrode configuration using an electrochemical workstation (CHI 660E, CH Instruments Inc.). The capacitance of the supercapacitors in a two-electrode cell was calculated from their GCD curves at different current densities using

$$C = I\,\Delta t/\Delta U \tag{1}$$

where C is the total capacitance, I and Δt are the discharging current and time, respectively, ΔU is the potential window after IR drop.

The areal and volumetric capacitances (C_A and C_V) of the SCs were calculated according to the equations

$$C_A = C/A \tag{2}$$

$$C_V = C/V \tag{3}$$

where A and V refer to the area and volume of the fiber in both electrodes, respectively. The calculation of A and V is according to the equations:

$$A = 2\pi DL \tag{4}$$

$$V = 2\pi R^2 L \tag{5}$$

where D and R are the diameter and radius of the fiber, respectively, L is the fiber length, factor 2 means two fibers.

The volumetric energy density (E_V, Wh cm^{-3}) and power density (P_V, W cm^{-3}) of the SCs were obtained from the equation:

$$E_V = 0.5\,C_V \Delta U^2 \Big/ 3600 \tag{6}$$

$$P_V = E_V \times 3600 \Big/ t_{discharge} \tag{7}$$

where ΔU is the operating voltage window in volts, $t_{discharge}$ is the discharge time in seconds.

3. Results and discussions

The MnO_2 nanowires were prepared by a low temperature hydrothermal method. The phase purity and crystal structure of the MnO_2 nanowires were examined by XRD. As shown in Fig. 1a, all the diffraction peaks can be exclusively indexed as the tetragonal α-MnO_2 (JCPDS 44-0141), and no other impurities are observed [25]. The broad characteristic peaks in the XRD patterns indicates the poor crystallinity of the α-MnO_2. Fig. 1b shows the SEM image of the as-prepared α-MnO_2, which exhibits nanowire morphology with diameters of 5–20 nm and lengths ranging between 5 and 10 μm. A lattice spacing about 0.701 nm for (110) planes of the tetragonal α-MnO_2 structure along the nanowire can be readily resolved in Fig. 1c and the crystallinity is not very high, as consistent with the XRD results. In fact, MnO_2 with low crystallinity is more favorable for SC application compared with the high crystalline MnO_2 due to the easier penetration of ions through it [26,27]. We prepared homogeneous MnO_2/GO hybrid dispersions with 5 wt%, 10 wt%, 20 wt%, 30 wt% and 40 wt% nanowires respecting to the total weight of GO and MnO_2. As shown by the low magnification TEM image of GO/MnO_2 hybrid dispersions (Fig. 1d), the MnO_2 nanowires are well wrapped by GO sheets which can effectively inhibit their aggregation and increase the mass loading.

We prepared MnO_2/rGO hybrid fibers by a simple wet spinning method followed by chemical reduction. The homogeneous dispersion was smoothly injected into a rotating coagulation bath through a spinneret. The mass loading of MnO_2 nanowires can be well controlled by adjusting the content of MnO_2 in the spinning dispersion. By this method, hundreds of meters long MnO_2/GO hybrid fiber can be obtained (Fig. 2a). However, continuous fibers could not be formed when the fraction of MnO_2 was over 40 wt%. In order to obtain MnO_2/rGO fibers, modified vapor reduction method was employed, by exposing the MnO_2/GO fiber to the hydrazine vapor.

The physical properties of rGO and MnO_2/rGO fibers are listed in Table 1. Stress–strain curves (Fig. S2) of the prepared fibers indicates that the mechanical strength decreases with the increasing MnO_2 content. The decline on strength can be attributed to the fact that the MnO_2 nanowires between the graphene nanosheets inhibited the aggregation and increased the layer distance which reduced the van der Waals forces between graphene nanosheets and thus reduced the tensile strength. This can also explain why the diameter of the fibers increases with the increasing content of MnO_2. Due to the loading of low conductivity MnO_2, the conductivity of the fibers decreases with the increasing content of MnO_2.

The microstructure of MnO_2/rGO-40 fiber was characterized by SEM (Fig. 2 b–c). A 3-dimensional interconnected porous network structure formed by crumpled graphene sheets can be clearly observed from the cross-section of the fiber (Fig. 2c). This type of porous structure provides large accessible surface area that enables effective electrolyte ion transport. Fig. 2d–f shows the energy-dispersive spectroscopy (EDS) mapping of the cross section of the hybrid fiber, demonstrating the existence of C, O and Mn elements. The distribution of Mn element confirms that MnO_2 nanowires are homogeneously distributed throughout the hybrid fiber, which is crucially important for increasing the mass loading and usage of MnO_2 nanowires and improving the electrochemical performances of the hybrid fiber-based SC.

Fig. 3a shows the Raman spectra of the rGO and MnO_2/rGO-40 fiber. The defect induced D peak and G peak can be found at around 1335 cm^{-1} and 1585 cm^{-1}, respectively, for both of these fibers. As for the MnO_2/rGO-40 fiber, a new peak appeared at 641 cm^{-1}, which can be attributed to the Mn–O stretching vibration in the basal plane of MnO_6 octahedra, indicating the presence of MnO_2 in the hybrid fiber as well [28]. X-ray photoelectron spectra (XPS) was

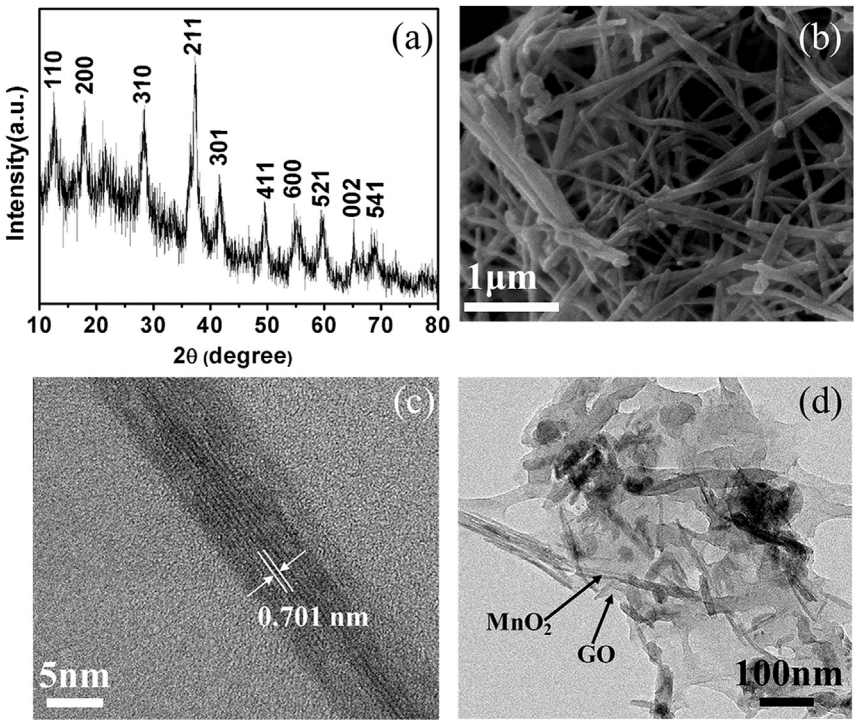

Fig. 1. (a–c) XRD pattern, SEM image and high resolution TEM image of the MnO_2 nanowires; (d) TEM image of a MnO_2/GO hybrid dispersion.

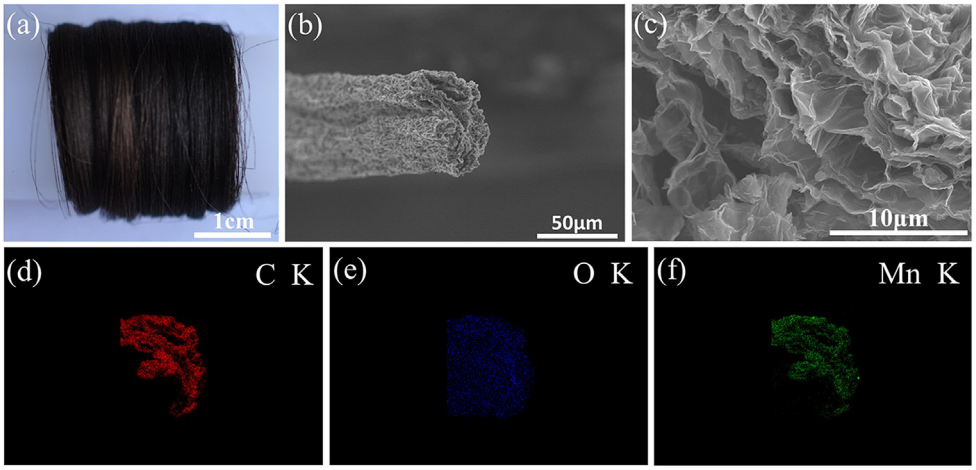

Fig. 2. (a) Photograph of the MnO_2/GO fiber collected onto a bobbin; (b–f) Cross-sectional SEM images (b, c) and element mappings (d-f for C, O and Mn, respectively) of MnO_2/rGO-40 fiber.

Table 1
Physical properties of rGO and MnO_2/rGO fibers.

Fibers	Diameter (μm)	Surface area ($m^2\ g^{-1}$)	Strength (MPa)	Strain (%)	Conductivity (S cm^{-1})
rGO fiber	38 ± 2	35.8	118	4.4	26.4
MnO_2/rGO-5 fiber	40 ± 2	40.9	117	4.8	25.2
MnO_2/rGO-10 fiber	42 ± 2	70.3	109	6.4	24.8
MnO_2/rGO-20 fiber	45 ± 2	92.0	93	6.1	24.1
MnO_2/rGO-30 fiber	46 ± 2	108.2	85	8.0	22.0
MnO_2/rGO-40 fiber	49 ± 2	139.9	75	3.7	18.3

used to identify the presence and oxidation state of the as prepared MnO_2 nanowires in the hybrid fibers. As shown in Fig. 3b, the C 1s signal was deconvoluted into four peaks centered at 284.4, 285.6, 288.1 and 290.6 eV, corresponding to C–C/C=C, C–N, C=O and O=C–O bonds, respectively. The C–N bond may be introduced during the reduction process by hydrazine [29]. The intensity of the peaks related to oxygenate bonds are rather low, indicating the successful reduction of GO. As for the O 1s signal (Fig. 3c) two deconvoluted

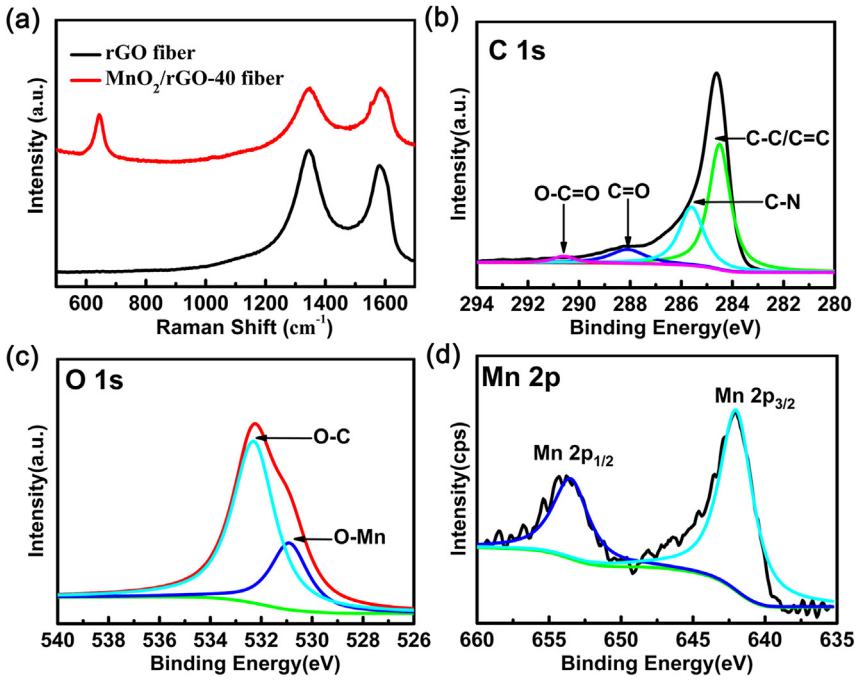

Fig. 3. (a) Raman spectra of rGO and MnO_2/rGO-40 fiber; (b) C 1s; (c) O 1s; and (d) Mn 2p XPS core level spectra of MnO_2/rGO-40 fiber.

peaks centered at 530.9 and 532.3 eV were assigned to O–Mn and O–C bond, respectively [9]. The presence of MnO_2 in the hybrid fiber was further confirmed by the Mn 2p signal in Fig. 3d. The peaks of Mn $2p_{3/2}$ and Mn $2p_{1/2}$ are located at 641.9 and 653.6 eV, respectively, with an energy separation of 11.7 eV, which exactly matches the reported value of energy separation in MnO_2 [30].

In order to explore the surface area and porous structure of the rGO fiber and MnO_2/rGO hybrid fibers, we carried low-temperature nitrogen adsorption measurements. Fig. 4 shows the nitrogen adsorption and desorption isotherms and the pore size distribution curve of MnO_2/rGO-40 fiber. A significant increase in surface area is observed for the hybrid fiber compared to that of the rGO fiber (Table 1). The type IV isotherm shows a hysteresis loop at high relative pressure, indicating the existence of plentiful mesopores in the hybrid fiber (Fig. 4a). The BET surface area and pore-size distribution combined with the SEM image (Fig. 2c) strongly confirm the fact that the hybrid fibers have an interconnected porous structure. MnO_2 nanowires inserted between the graphene layers effectively reduce the stacking of the graphene and well develop interconnected pores in the hybrid fiber. The MnO_2/rGO-40 fiber has a specific surface area of 139.9 $m^2\ g^{-1}$, much higher than those of carbon-based fibers reported so far, including rGO fiber (18 $m^2\ g^{-1}$) [31] and dry-spun MWCNT fiber (100 $m^2\ g^{-1}$) [32], and comparable to wet-spun SWNT fiber (160 $m^2\ g^{-1}$) [33]. The pore size distribution, calculated from desorption data using the Barrett–Joyner–Halenda (BJH) model, ranges from 2.2 nm to 55 nm, indicating the mesoporous structure of the hybrid fiber (Fig. 4b). Such hierarchical structure with high specific surface area and mesopores is favorable for improving both the main pseudocapacitance of MnO_2 and the electric double-layer (EDL) capacitance of graphene since the hydrated ions in the electrolyte are easily accessible to the exterior and interior pore surfaces during the rapid charge–discharge process.

To fabricate fiber-based SCs, PVA-H_3PO_4 had been used as gel electrolyte. Firstly, rGO or MnO_2/rGO hybrid fibers were coated by the gel electrolyte, then two same fibers were twisted together to produce a fiber-based SC. In order to facilitate testing, we encapsulated it in a silicone tube. The electrochemical performance of the fiber-based SCs were analyzed by a two-electrode configuration. Fig. 5a depicts the typical CV curves of fiber-based SCs with different MnO_2 contents at the scan rate of 10 mV s^{-1}. The CV curves of the hybrid fibers are nearly rectangular in shape and exhibit near

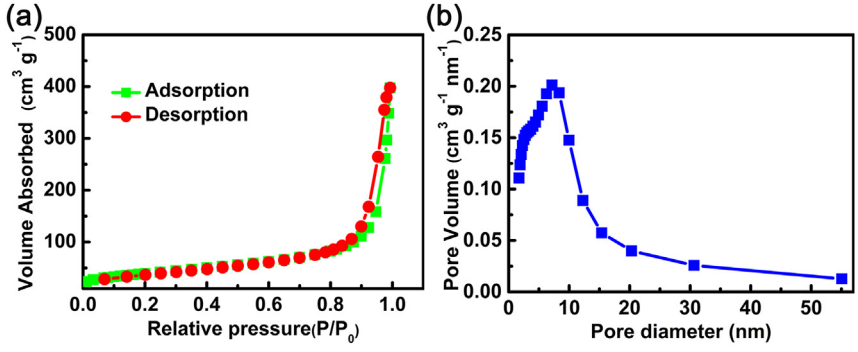

Fig. 4. Pore structure of MnO_2/rGO-40 fiber (a) Adsorption–desorption isotherms and (b) the pore-size distribution of the MnO_2/rGO-40 fiber.

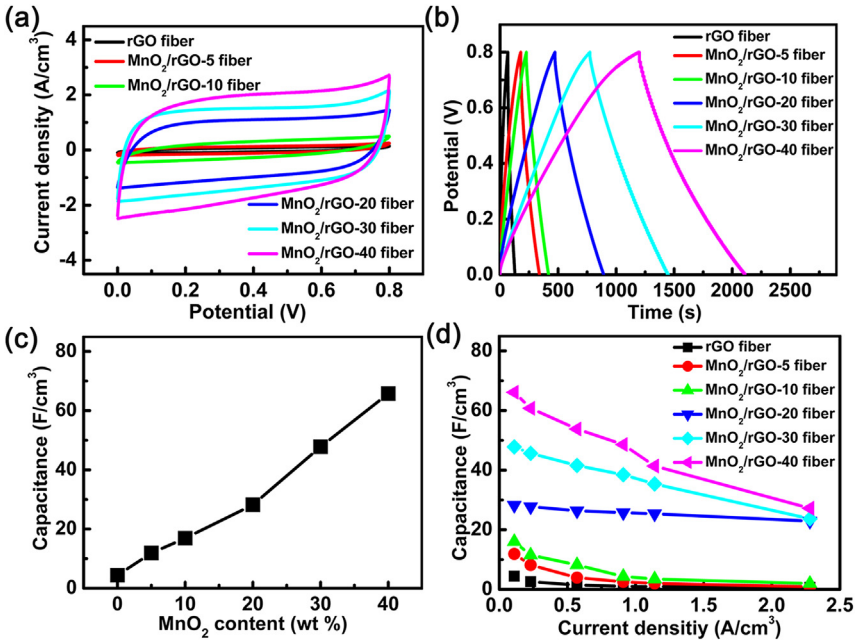

Fig. 5. Electrochemical performance of solid-state SCs assembled from rGO fiber and MnO_2/rGO hybrid fibers with different MnO_2 contents. (a) CV curves at a scan rate of 10 mV s^{-1}; (b) The GCD curves at a current density of 0.06 A cm^{-3}; (c) Volumetric capacitance with the increase of MnO_2 contents at a current density of 0.06 A cm^{-3}; (d) Volumetric capacitance with the increase of current density for fibers with different MnO_2 contents.

mirror-image symmetry, which demonstrates the ideal capacitive behavior. The area of each closed CV curve suggests its specific capacitance. It is found that the area increases with the increase of MnO_2 content, corresponding to an increase in the capacitance, which demonstrates that the capacitive behavior of graphene fibers can be greatly improved by loading of MnO_2 nanowires. GCD tests were conducted in a stable potential window of 0–0.8 V at a fixed current density of 0.06 A cm^{-3}, and the result is shown in Fig. 5b. It reveals that all of the charging curves are symmetrical with their corresponding discharge counterparts and show good linear voltage–time profiles, indicating good capacitive behavior of the fiber-based SCs. Fig. 5c indicates that the specific capacitance increases with the mass loading and no saturation are observed in the range of loadings suggesting almost all of the MnO_2 participated in the reactions and contributed to the energy storage. The dependence of specific capacitance on current density is also investigated (Fig. 5d). It was found that the hybrid fiber with 40% MnO_2 content has the highest C_V (normalized by the total volume of two fiber electrodes) of 66.1 F cm^{-3} at 60 mA cm^{-3} and 41.3 F cm^{-3} at 970 mA cm^{-3}, corresponding to C_A of 82.6 F cm^{-2} and 51.4 mF cm^{-2}, respectively. These values outperform those of previously reported fiber-based SCs, including RGO/CNT fiber [16,34], MnO_2-modified graphene fiber [21,22], MnO_2/Carbon fiber and CNT/MnO_2 fiber [8,35] (Table 2). Meanwhile, the SC also exhibited better rate capability when current density increases from 0.06 to 2.28 A cm^{-3} compared with rGO fiber-based SC. The high rate performance could be attributed to the interconnected porous structure of the hybrid fiber, which could allow electrolyte ions to pass through quickly during the rapid charge/discharge process.

To further investigate the electrochemical performance of these MnO_2/rGO hybrid fiber electrodes, we take MnO_2/rGO-40 fiber as the example to study. Fig. 6a shows the CV curves of the device measured at different scan rates of 10, 20, 50 and 100 mV s^{-1}. These CV curves exhibit near-rectangular shapes at low scan rates and still retain a relatively rectangular shape without obvious distortion with increasing scan rates, indicating the desirable fast charge/discharge property for power devices. The GCD curves at different current densities ranging from 0.06 to 2.28 A cm^{-3} were shown in Fig. 6b, through which good linear potential-time profiles were achieved, demonstrating a good capacitive performance of the devices. The Ragone plots in Fig. 6c compare the volumetric performance of our device to those of rGO fiber-based SC and commercially available energy-storage devices. Our device has an E_V of 5.8 mWh cm^{-3}, which is about 6.7 times higher than rGO fiber-based SC, ten times higher than commercially available SCs (2.75 V/44 mF and 5.5 V/100 mF, <1 mWh cm^{-3}) [36,37] and even comparable to the 4 V/500 μAh thin-film lithium battery (0.3–10 mWh cm^{-3}) [38]. This energy density value is also higher than that of many previously reported graphene fiber-based SCs, including RGO + CNT@CMC YSCs (3.5 mWh cm^{-3}) [16],

Table 2
Comparison of electrochemical performance of hybrid fiber-based supercapacitors.

Ref.	Electrode materials	C_V (F cm^{-3})	C_A (mF cm^{-2})	P_V (mW cm^{-3})	E_V (mWh cm^{-3})
[16]	RGO/CNT fiber	38.4	44.25	200	3.5
[34]	RGO/CNT fiber	38.8	–	500	3.4
[21]	RGO fiber/MnO_2	42.25	14.8	16.8	3.4
[22]	RGO fiber/MnO_2	–	9.6	–	–
[8]	Carbon fiber/MnO_2	2.5		400	0.22
[35]	CNT fiber/MnO_2	–	3.57	790	1.73
This work	MnO_2 nanowire/rGO-40 fiber	66.1	82.6	510	5.8

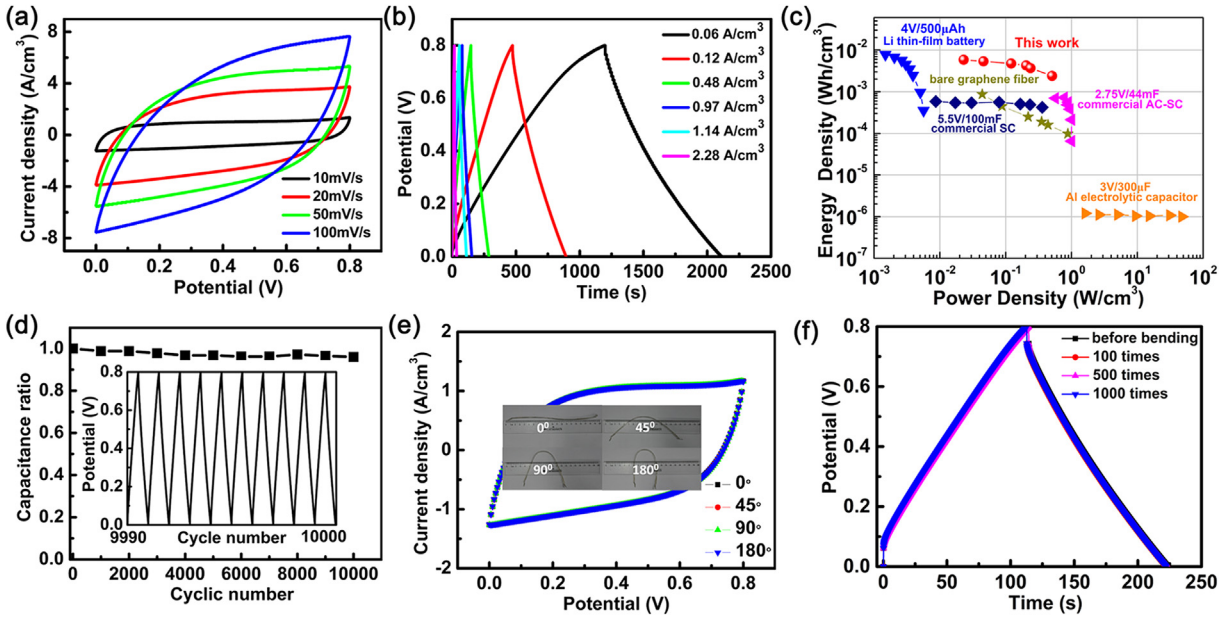

Fig. 6. Electrochemical performances of solid-state SC assembled from MnO_2/rGO-40 fiber. (a) CV curves of the SC at different scan rates; (b) The GCD curves of the SC at different current densities; (c) Energy and power densities of the SC compared with commercially available energy-storage systems; (d) Dependence of capacitance ratio on cycle number. Inset: GCD curve after 10000 cycles at 0.12 A cm^{-3} (e) CV curves under bending at with different angles; (f) GCD curves before and after bending for 100, 500 and 1000 cycles.

RGO + unfunctionalized few-walled CNT fiber-based SC (1 mWh cm^{-3}) [34] and MnO_2 decorated graphene fiber-based asymmetric micro-SCs [21] and an asymmetric SC assembled from N-doped and MnO_2-loaded RGO/SWCNT fibers (~5 mWh cm^{-3}) [39], and also comparable with that of a N-doped RGO/SWCNT hybrid fiber SC (~6.3 mWh cm^{-3}) [15]. The maximum P_V of our SC is 510 mW cm^{-3}, comparable to the commercially available supercapacitors and more than two orders of magnitude higher than that of lithium thin-film batteries [37,38]. The cycle stability was measured by GCD at a current density of 0.12 A cm^{-3} for 10000 cycles and the result is shown in Fig. 6d. The capacitance retention was about 96% after cycling for 10000 times, demonstrating the excellent long-term cycling stability. The inset reveals no significant electrochemical change during the long-term charging and discharging process. The excellent electrochemical stability indicates that the graphene nanosheets wrapping could possibly stabilize the MnO_2 nanowires mechanically during the cycling tests. In order to demonstrate the flexibility of our device, we measured CV curves under different bending angles and GCD curves after different bending times. The CV curves in Fig. 6e demonstrate that the change of electrochemical performance of the fabricated device was ignorable under different bending angles. From the GCD curves of the device after different bending times (Fig. 6f), almost no change for the charge–discharge curves was observed during the bending. All of these datas prove that the device is flexible and robust enough to tolerate the long-term and repeated bending.

For practical application, flexible electronics may need working at different currents and operation voltages. Thus, depending on the application, SCs need to be connected together in series and/or parallel combinations. Fig. 7a,b show the GCD curves of a single and three devices connected in parallel and series. Compared with a single device, the output current of the three devices connected in parallel increased by a factor of three and its discharge time is three times that of a single device when operated at the same current density (Fig. 7a). With similar discharge time, the voltage window can be elevated from 0.8 V for single device to 2.4 V by connecting three device in series (Fig. 7b). After being fully charged, the device connected in series can be used to power a red LED even under knotting state as shown in Fig. 7c, demonstrating its potential application as an efficient energy storage component for flexible electronics.

The observed excellent electrochemical performances of the as-prepared SC can be ascribed to the following factors: (1) The hybrid fibers have multiscale hierarchical structure mainly with mesopores, in addition to their high electrical conductivity, superior mechanical properties, good electrochemical stability, and high surface area. This structure provides pores and large accessible surface area for fast hydrate ion transport and storage. (2) The synergistic effect between MnO_2 nanowires and graphene. Highly conductive graphene wrapping around the MnO_2 nanowires can inhibit the aggregation of MnO_2 nanowires and increase their mass loading. Meanwhile, highly conductive graphene serve as superhighways can improve charge transfer of MnO_2, facilitate the electron transport in the fiber and improve the electrochemical utilization of MnO_2 nanowires. MnO_2 nanowires not only act as an effective spacer to inhibit the restacking of graphene nanosheets and form hierarchical structure, which can provide a large surface area with well-defined mesopores for efficient electrolyte penetration and ion adsorption, but also provide pseudo capacitance to improve the overall performance. The one-dimensional structure of MnO_2 nanowires with small diameters is also helpful for shortening ion diffusion path, which can greatly reduce the ionic diffusion resistance and charge transfer resistance.

4. Conclusions

In summary, a novel hybridization strategy for fabricating porous graphene-based fibers is proposed. Flexible freestanding MnO_2 nanowire/rGO fibers with interconnected porous structure was prepared by a simple wet-spinning process combined with chemical reduction and a solid-state SC based on MnO_2 nanowire/rGO hybrid fibers was successfully obtained. The loading content of MnO_2 in the precursor fiber can be easily controlled to be as high as

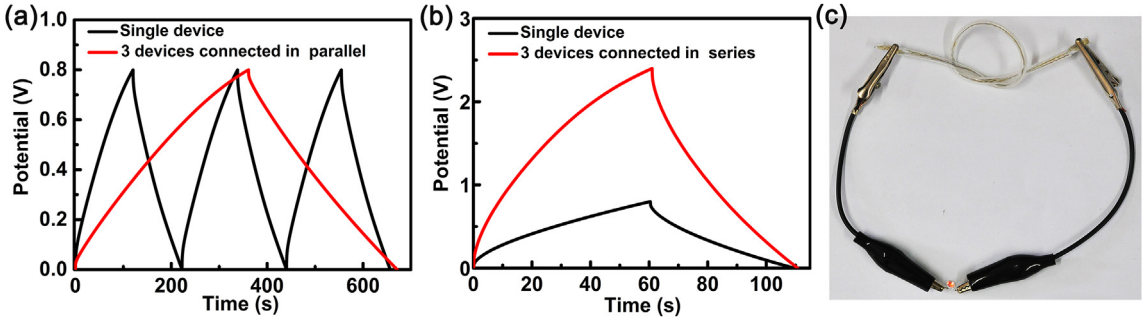

Fig. 7. GCD curves of single and three devices connected in parallel (a) and series (b); (c) Photograph showing three as prepared devices connected in series driving a red LED (1.8 V, 20 mA) under the knotting state.

40 wt%. It was found that the specific capacitance and rate performance of these fibers increased obviously with the increase of MnO_2 content. A flexible solid-state SC assembled from the hybrid fiber with the highest MnO_2 content exhibited very high volumetric capacitance (66.1 F cm^{-3}), excellent cycling stability (96% capacitance retention over 10000 cycles), and high energy and power density (5.8 mWh cm^{-3} and 0.51 W cm^{-3}, respectively). It also well maintained its physical shape and electrochemical performance under long-time periodical mechanical deformation. In addition, this strategy presented here can be extended to the rational design of other one-dimensional nanomaterials/rGO hybrid fibers, which may be promising for the next generation flexible energy storage devices.

Acknowledgments

We would like to thank the financial supports from Natural Science Foundation of China (51273040), Program for Changjiang Scholars and Innovative Research Team in University (T2011079, IRT1221), and National Natural Science Foundation for Distinguished Young Scholar of China (50925312), and Fundamental Research Funds for the Central Universities (2232015D3-20).

Appendix A. Supplementary data

Supplementary data related to this article can be found at http://dx.doi.org/10.1016/j.jpowsour.2015.12.063.

References

[1] D.-H. Kim, N. Lu, R. Ma, Y.-S. Kim, R.-H. Kim, S. Wang, J. Wu, S.M. Won, H. Tao, A. Islam, K.J. Yu, T.-i. Kim, R. Chowdhury, M. Ying, L. Xu, M. Li, H.-J. Chung, H. Keum, M. McCormick, P. Liu, Y.-W. Zhang, F.G. Omenetto, Y. Huang, T. Coleman, J.A. Rogers, Science 333 (2011) 838–843.
[2] M. Koo, K.-I. Park, S.H. Lee, M. Suh, D.Y. Jeon, J.W. Choi, K. Kang, K.J. Lee, Nano Lett. 12 (2012) 4810–4816.
[3] V.L. Pushparaj, M.M. Shaijumon, A. Kumar, S. Murugesan, L. Ci, R. Vajtai, R.J. Linhardt, O. Nalamasu, P.M. Ajayan, Proc. Natl. Acad. Sci. 104 (2007) 13574–13577.
[4] K. Jost, D. Stenger, C.R. Perez, J.K. McDonough, K. Lian, Y. Gogotsi, G. Dion, Energ Environ. Sci. 6 (2013) 2698–2705.
[5] Z. Weng, Y. Su, D.-W. Wang, F. Li, J. Du, H.-M. Cheng, Adv. Energy Mater. 1 (2011) 917–922.
[6] P. Simon, Y. Gogotsi, Nat. Mater 7 (2008) 845–854.
[7] X. Yang, C. Cheng, Y. Wang, L. Qiu, D. Li, Science 341 (2013) 534–537.
[8] X. Xiao, T. Li, P. Yang, Y. Gao, H. Jin, W. Ni, W. Zhan, X. Zhang, Y. Cao, J. Zhong, L. Gong, W.C. Yen, W. Mai, J. Chen, K. Huo, Y.-L. Chueh, Z.L. Wang, J. Zhou, ACS Nano 6 (2012) 9200–9206.
[9] Z.S. Wu, W. Ren, D.-W. Wang, F. Li, B. Liu, H.-M. Cheng, Acs Nano 4 (2010) 5835–5842.
[10] Z. Xu, H. Sun, X. Zhao, C. Gao, Adv. Mater. 25 (2013) 188–193.
[11] Z. Xu, Z. Liu, H. Sun, C. Gao, Adv. Mater. 25 (2013) 3249–3253.
[12] S. Chen, W. Ma, Y. Cheng, Z. Weng, B. Sun, L. Wang, W. Chen, F. Li, M. Zhu, H.-M. Cheng, Nano Energy 15 (2015) 642–653.
[13] G. Huang, C. Hou, Y. Shao, H. Wang, Q. Zhang, Y. Li, M. Zhu, Sci. Rep. 4 (2014) 4248.
[14] M. Li, Z. Tang, M. Leng, J. Xue, Adv. Funct. Mater. 24 (2014) 7495–7502.
[15] D. Yu, K. Goh, H. Wang, L. Wei, W. Jiang, Q. Zhang, L. Dai, Y. Chen, Nat. Nano 9 (2014) 555–562.
[16] L. Kou, T. Huang, B. Zheng, Y. Han, X. Zhao, K. Gopalsamy, H. Sun, C. Gao, Nat. Commun. 5 (2014) 3754.
[17] Z.J. Fan, J. Yan, T. Wei, L.J. Zhi, G.Q. Ning, T.Y. Li, F. Wei, Adv. Funct. Mater. 21 (2011) 2366–2375.
[18] Y. Meng, K. Wang, Y. Zhang, Z. Wei, Adv. Mater. 25 (2013) 6985–6990.
[19] Z.-S. Wu, G. Zhou, L.-C. Yin, W. Ren, F. Li, H.-M. Cheng, Nano Energy 1 (2012) 107–131.
[20] G. Yu, L. Hu, N. Liu, H. Wang, M. Vosgueritchian, Y. Yang, Y. Cui, Z. Bao, Nano Lett. 11 (2011) 4438–4442.
[21] B. Zheng, T. Huang, L. Kou, X. Zhao, K. Gopalsamy, C. Gao, J. Mater Chem. A 2 (2014) 9736–9743.
[22] Q. Chen, Y. Meng, C. Hu, Y. Zhao, H. Shao, N. Chen, L. Qu, J. Power Sources 247 (2014) 32–39.
[23] T.M. Higgins, D. McAteer, J.C.M. Coelho, B.M. Sanchez, Z. Gholamvand, G. Moriarty, N. McEvoy, N.C. Berner, G.S. Duesberg, V. Nicolosi, J.N. Coleman, Acs Nano 8 (2014) 9567–9579.
[24] W.S. Hummers, R.E. Offeman, J. Am. Chem. Soc. 80 (1958) 1339.
[25] X. Wang, Y. Li, J. Am. Chem. Soc. 124 (2002) 2880–2881.
[26] L. Bao, J. Zang, X. Li, Nano Lett. 11 (2011) 1215–1220.
[27] Z. Zhang, F. Xiao, L. Qian, J. Xiao, S. Wang, Y. Liu, Adv. Energy Mater. 4 (2014) 1400064.
[28] A. Sumboja, C.Y. Foo, X. Wang, P.S. Lee, Adv. Mater. Deerf. Beach, Fla. 25 (2013) 2809–2815.
[29] S. Stankovich, D.A. Dikin, R.D. Piner, K.A. Kohlhaas, A. Kleinhammes, Y. Jia, Y. Wu, S.T. Nguyen, R.S. Ruoff, Carbon 45 (2007) 1558–1565.
[30] S.W. Lee, J. Kim, S. Chen, P.T. Hammond, Y. Shao-Horn, ACS Nano 4 (2010) 3889–3896.
[31] H. Cheng, Z. Dong, C. Hu, Y. Zhao, Y. Hu, L. Qu, N. Chen, L. Dai, Nanoscale 5 (2013) 3428–3434.
[32] X.L. Chen, L.B. Qiu, J. Ren, G.Z. Guan, H.J. Lin, Z.T. Zhang, P.N. Chen, Y.G. Wang, H.S. Peng, Adv. Mater. 25 (2013) 6436–6441.
[33] A.V. Neimark, S. Ruetsch, K.G. Kornev, P.I. Ravikovitch, Nano Lett. 3 (2003) 419–423.
[34] Y. Ma, P. Li, J.W. Sedloff, X. Zhang, H. Zhang, J. Liu, Acs Nano 9 (2015) 1352–1359.
[35] J. Ren, L. Li, C. Chen, X.L. Chen, Z.B. Cai, L.B. Qiu, Y.G. Wang, X.R. Zhu, H.S. Peng, Adv. Mater. 25 (2013) 1155–1159.
[36] M.F. El-Kady, R.B. Kaner, Nat. Commun. 4 (2013) 1475.
[37] M.F. El-Kady, V. Strong, S. Dubin, R.B. Kaner, Science 335 (2012) 1326–1330.
[38] D. Pech, M. Brunet, H. Durou, P. Huang, V. Mochalin, Y. Gogotsi, P.-L. Taberna, P. Simon, Nat. Nano 5 (2010) 651–654.
[39] D. Yu, K. Goh, Q. Zhang, L. Wei, H. Wang, W. Jiang, Y. Chen, Adv. Mater. 26 (2014) 6790–6797.